


Article

Bi₂WO₆@g-C₃N₄ Heterostructure for Cathodic Photoelectrochemical Dopamine Sensor

Zhifang Wu ¹, Ying Su ¹, Fangjie Han ¹, Zhishan Liang ¹, Dongxue Han ^{1,2,*}, Dongdong Qin ^{1,*} and Li Niu ¹ 

¹ Guangzhou Key Laboratory of Sensing Materials and Devices, Guangdong Engineering Technology Research Center for Photoelectric Sensing Materials and Devices, School of Chemistry and Chemical Engineering, Guangzhou University, Guangzhou 510006, China; fjhan@gzhu.edu.cn (F.H.); lniu@gzhu.edu.cn (L.N.)

² Guangdong Provincial Key Laboratory of Psychoactive Substances Monitoring and Safety, Anti-Drug Tethology Center of Guangdong Province, Guangzhou 510230, China

* Correspondence: dxhan@gzhu.edu.cn (D.H.); ccqindd@gzhu.edu.cn (D.Q.)

Abstract: A simple and low-cost cathodic photoelectrochemical (PEC) sensor based on Bi₂WO₆@g-C₃N₄ was designed for dopamine (DA) detection. The Bi₂WO₆ nanoflower was first prepared using a simple hydrothermal method followed by the combination with g-C₃N₄ nanosheet to form the Bi₂WO₆@g-C₃N₄ heterostructure. The heterostructure can extend the absorbance to the visible region and accelerate the transfer of charge carriers. Furthermore, DA easily coordinates with exposed Bi³⁺ on the Bi₂WO₆ surface and forms the charge-transfer complex to further enhance the cathodic photocurrent. Under optimal conditions, there are two linear relationships between the concentration of DA and photocurrent intensity. The linear ranges are 0.1–10 μM and 10–250 μM, with a sensitive detection limit (LOD) of 28 nM. Notably, the real sample of human blood serum analysis further revealed the accuracy and feasibility of the Bi₂WO₆@g-C₃N₄-based PEC platform. Convincingly, the heterostructure of Bi₂WO₆ and g-C₃N₄ opened up a new avenue for the construction of DA analysis.

Keywords: photoelectrochemical; Bi₂WO₆@g-C₃N₄; dopamine sensor; human serum



Citation: Wu, Z.; Su, Y.; Han, F.; Liang, Z.; Han, D.; Qin, D.; Niu, L. Bi₂WO₆@g-C₃N₄ Heterostructure for Cathodic Photoelectrochemical Dopamine Sensor. *Chemosensors* **2023**, *11*, 404. <https://doi.org/10.3390/chemosensors11070404>

Academic Editor: Ambra Giannetti

Received: 29 June 2023

Revised: 14 July 2023

Accepted: 17 July 2023

Published: 19 July 2023



Copyright: © 2023 by the authors. Licensee MDPI, Basel, Switzerland. This article is an open access article distributed under the terms and conditions of the Creative Commons Attribution (CC BY) license (<https://creativecommons.org/licenses/by/4.0/>).

1. Introduction

Dopamine (DA) is an important neurotransmitter that plays a key role in the function of the human central nervous, metabolism, renal, immune and cardiovascular systems [1,2]. DA levels in biological systems have attracted much attention in the clinical field due to abnormal changes in DA concentrations being closely associated with many serious physical and neurological disorders [3,4]. Inadequate levels of DA in the brain may lead to neurological disorders such as schizophrenia and attention deficit hyperactivity disorder [5]. On the other hand, higher levels of DA may lead to pleasure and euphoria [6]. Therefore, the high precision and rapid measurement of DA concentrations are important for the diagnosis and treatment of related disorders.

To date, a number of analytical technologies have been developed for DA detection, such as electrochemiluminescence [7], fluorescence spectrophotometry (FL) [8], high-performance liquid chromatography [9], and electrochemical method (EC) [10–12]. It is a pity that most of these methods more or less required sophisticated equipment and were affected by external circumstances and a lack of portability. In recent years, photoelectrochemical (PEC) sensors have blossomed into promising analysis methods with the advantages of EC, such as simple equipment, fast response speed, and being easy-to-operate [13,14]. Owing to the partition of the excitation and detection signal, the PEC sensing exhibits high sensitivity and a lower detection limit than the EC sensor [15–17]. And the selection of photoelectric materials is a major key subject in the fabrication of PEC sensors.

Bi₂WO₆ is an attractive aurivillius oxide that has been widely used in the fields of sensors, photocatalysis, and environmental remediation of wastewater due to its stable

physicochemical properties [18–20]. However, the low absorption efficiency of pure Bi_2WO_6 for light and the poor transfer efficiency for electrons are major challenges to further improve the performance of PEC. In the quest for promoting electron(e^-)-hole(h^+) pairs separation and suppressing unnecessary carrier recombination effects, researchers have made great efforts in tuning the physical morphology and regulating the chemical composition. Undoubtedly, the hierarchical structure brings numerous advantages, and researchers have prepared a variety of Bi_2WO_6 with different morphologies in recent years, such as single-crystal-like [21], helix-like [22], 3D microspheres [23] and 3D flower-like Bi_2WO_6 [24]. These unique structures can effectively improve the aggregation of nanosheets, thereby exhibiting a larger specific surface area and endowing better photocatalytic performance. Among these 3D structures, the flower-like Bi_2WO_6 displays a large surface area and outstandingly facilitates the separation of photogenerated charge carriers. Composition tuning mainly focuses on noble metal loading [25], element doping [26], heterostructures [27] and so on. Currently, constructing a heterostructure with two proper energy band matching semiconductors as favorite photoelectrode schemes [28–30]. Adhikari et al. prepared $\text{Bi}_2\text{S}_3/\text{Bi}_2\text{WO}_6$ hierarchical microstructures that exhibited excellent performance for ofloxacin detection [31]. Zhang prepared $\text{Bi}_2\text{WO}_6/\text{TiO}_2$ flake nano-heterostructures catalysts, which possessed the high photocatalytic property for the degradation of methylene blue [32]. The above modification method has also demonstrated that the construction of heterojunctions can extend the absorbance to the visible region and more effectively hinder the recombination of carriers, thereby improving the performance of the sensor.

Graphite-like carbon nitride ($g\text{-C}_3\text{N}_4$) has become a research hotspot due to its numerous advantages such as inexpensive, easy synthesis and stable physical and chemical properties and has been widely used in lithium-ion batteries, energy conversion and storage and photocatalysis [33–35]. For instance, Zhao et al. established a PEC sensor based on $g\text{-C}_3\text{N}_4/\text{BiVO}_4$ heterostructure for tetracycline determination [36]. Cao et al. prepared a Cu-BTC MOF/ $g\text{-C}_3\text{N}_4$ nanosheet for the detection of non-electroactive glyphosate [37]. The usage of $g\text{-C}_3\text{N}_4$ to design heterojunction indeed greatly improves the performance of the sensor. However, reductive molecules tend to absorb at the n-type-based photoanode/electrolyte interface, which will inevitably affect the intrinsic hole oxidation reaction in real biological sample analysis [38].

Motivated by these concerns, the Bi_2WO_6 nanoflowers were first prepared using a simple hydrothermal method followed by the combination with $g\text{-C}_3\text{N}_4$ nanosheet to form the $\text{Bi}_2\text{WO}_6@g\text{-C}_3\text{N}_4$ heterostructure. The heterostructure showed better PEC performance than pure Bi_2WO_6 , which accelerated the transfer of charge carriers. More importantly, in the presence of DA, DA will replace water molecules and form the charge-transfer complex in concert with exposed Bi^{3+} , which is a key factor for enhanced cathodic photocurrent [39]. Moreover, the $\text{Bi}_2\text{WO}_6@g\text{-C}_3\text{N}_4$ -based PEC sensor obtained a good recovery in real human serum samples. Thus, the easily fabricated at a low-cost label-free PEC sensor based on $\text{Bi}_2\text{WO}_6@g\text{-C}_3\text{N}_4$ heterostructure achieves the selective detection of DA, which opened up a new avenue for the construction of DA analysis.

2. Materials and Methods

2.1. Reagents and Materials

The fluorine-doped tin oxide (FTO) glasses used as the substrates were purchased from Jinge-Wuhan and cut into $15 \times 25 \text{ mm}^2$ pieces before use. Bismuth nitrate pentahydrate ($\text{Bi}(\text{NO}_3)_3 \cdot 5\text{H}_2\text{O}$, 99%), sodium tungstate dihydrate ($\text{Na}_2\text{WO}_4 \cdot 2\text{H}_2\text{O}$) and urea were received from J&K Scientific Ltd. (Beijing, China). Ascorbic acid (AA), DA, uric acid (UA), L-proline (Pro), glutathione (GSH), L-cysteine (Cys), histidine (His) and glucose (Glu) were provided by InnoChem Science & Technology Co., Ltd. (Beijing, China). All reagents were used without further purification.

2.2. Apparatuses

In this work, a scanning electron microscope (SEM, JSM-7001F, Hitachi, Tokyo, Japan) and transmission electron microscope (TEM, JSM-2100F, JEOL, Tokyo, Japan) were used to observe the surface morphology and lattice spacing of the samples. The crystal structure information was studied using the X-ray diffractometer (XRD, Rigaku Ultima IV, Tokyo, Japan) with Cu K α radiation ($\lambda = 0.15405$ nm). X-ray photoelectron spectroscopy (XPS, Thermo Fischer ESCALAB Xi⁺, Waltham, MA, USA) was employed to characterize the surface chemical states of the samples. The vacuum level of the analysis chamber was 8×10^{-10} Pa, and the excitation source was Al K α rays ($h\nu = 1486.6$ eV). UV-vis diffuse reflectance spectra (DRS) of the samples were recorded on a UV-vis spectrophotometer (U-3900, Hitachi, Tokyo, Japan). The Fourier transform infrared (FTIR) spectra were carried out by an FTIR Spectrometer (Thermo Nicolet iS50, Waltham, MA, USA). A 420 nm LED light (Beijing Perfectlight Technology Co., Ltd., Beijing, China) was used as the irradiation source. All electrochemical experiments were carried out on the electrochemical workstation (CHI660E, Shanghai, China).

2.3. Syntheses of Bi₂WO₆@g-C₃N₄ Composites

The g-C₃N₄ was prepared using the reported heat-condensation polymerization method [35]. Quite simply, 10 g of urea was ground and placed in a tube furnace and maintained at a heating rate of 5 °C/min to 550 °C for 4 h. After natural cooling, the resulting pale yellow solid g-C₃N₄ was ground and prepared for use.

Bi₂WO₆ nanoflower structures (Bi₂WO₆ NFs) were synthesized using a conventional hydrothermal method [40]. In a typical process, 0.33 g of Na₂WO₄•2H₂O was dissolved in 20 mL of deionized (DI) water, labeled as solution A. And 0.97 g of Bi(NO₃)₃•5H₂O was prepared in another 20 mL of DI water, labeled as solution B. Solution B was then slowly added dropwise to solution A. The pH of the mixed solution was adjusted to 1 and stirring was continued for another 1 h. Subsequently, the final mixture solution was transferred to a 100 mL Teflon-lined stainless-steel autoclave and heated at 160 °C for 15 h. The reaction was brought to an end, and the reactor was allowed to cool naturally to room temperature. The obtained precipitate was washed through centrifugation with water and ethanol and then collected. The obtained precipitate was dried under a vacuum at 60 °C and ground into homogeneous pellets.

A certain amount of g-C₃N₄ (5 mg, 10 mg, 15 mg) was dispersed into 20 mL of DI water and sonicated for 1 h. Subsequently, 100 mg of the above-prepared Bi₂WO₆ NFs powder was weighed into the dispersion and stirred for 1 h. The purpose of stirring is to allow better contact between Bi₂WO₆ and g-C₃N₄ to form a more homogeneous complex. Then precipitate was separated through centrifugation and dried. The obtained samples were labeled as BWO-0.05CN, BWO-0.1CN and BWO-0.15CN, respectively.

2.4. Fabrication of Bi₂WO₆@g-C₃N₄/FTO PEC Sensor

Next, 100 μ L of 2 mg/mL Bi₂WO₆@g-C₃N₄ sample was dropped on FTO electrode with an active area of 0.785 cm², prepared using waterproof tape with a 1.0 cm diameter hole of. The performance of the same Bi₂WO₆@g-C₃N₄/FTO electrode was tested under optimal conditions. Bi₂WO₆@g-C₃N₄/FTO was placed as the working electrode in a homemade PEC detection cell containing 4 mL of 0.1 M PBS solution, together with Ag/AgCl used as the reference electrode and Pt wire used as the counter electrode to form a three-electrode detection system. The PEC detection was performed on a CHI660e electrochemical workstation, and data were recorded using the current-time (i-t) technique type at a bias potential of 0 V. A 420 nm LED was used as the irradiation source. After the dark current signal was stabilized, the photocurrent signal was collected by switching the light on and off alternately for 10 s three times. Different concentrations of DA were added continuously to the test cell for detection.

3. Results and Discussion

3.1. Morphology Characterization of $\text{Bi}_2\text{WO}_6@g\text{-C}_3\text{N}_4$ Composites

The synthetic strategy of the $\text{Bi}_2\text{WO}_6@g\text{-C}_3\text{N}_4$ sample is illustrated in Figure 1, which involves two steps. The Bi_2WO_6 nanoflower was first prepared using a simple hydrothermal method followed by the combination with $g\text{-C}_3\text{N}_4$ nanosheet to form the $\text{Bi}_2\text{WO}_6@g\text{-C}_3\text{N}_4$ heterostructure. The morphology, microstructure and lattice structure of BWO-0.1CN heterostructure were first investigated through SEM, TEM and HRTEM. Figure 2A shows that the Bi_2WO_6 obtained hydrothermally were uniform, and individual particles had a diameter of 2 μm . The higher magnification SEM image in Figure 2B presents that Bi_2WO_6 particles possess a 3D flower-like structure formed by numerous nanosheets with a thickness of several nanometers, which can greatly increase the surface area and active site of the samples. After the recombination with $g\text{-C}_3\text{N}_4$, it can be seen from Figure 2C that some of the $g\text{-C}_3\text{N}_4$ nanosheets grow on the Bi_2WO_6 nanoflower, and others disperse between the nanoflowers. Furthermore, the HRTEM image was further employed to confirm the formation of the $\text{Bi}_2\text{WO}_6@g\text{-C}_3\text{N}_4$ heterostructure. As shown in Figure 2D, some of the amorphous phases decorate the surface of the high crystallinity phase with an obvious interface, indicating its heterostructure character. The lattice spacing of about 0.315 nm belongs to the spacing of the (113) plane of orthogonal Bi_2WO_6 [40], while the amorphous phase with no clear lattice fringe is observed mainly due to the disordered state of $g\text{-C}_3\text{N}_4$. In addition, EDS-mapping (Figure 2E) shows that Bi, W, O, C and N elements are uniformly dispersed on the $\text{Bi}_2\text{WO}_6@g\text{-C}_3\text{N}_4$, which further clarifies the reliability of the heterostructure.

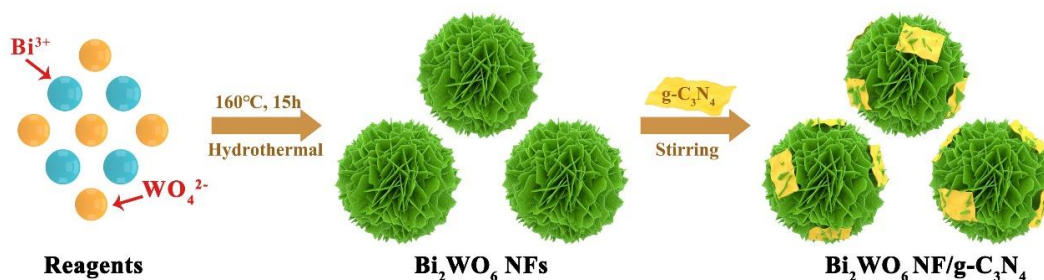


Figure 1. The preparation of Bi_2WO_6 NFs and Bi_2WO_6 NFs/ $g\text{-C}_3\text{N}_4$ composites.

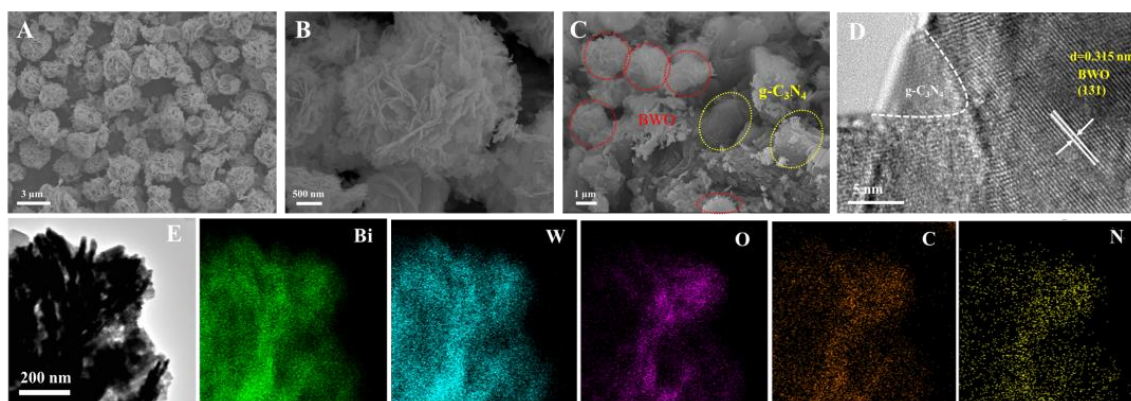


Figure 2. SEM image of (A,B) Bi_2WO_6 (BWO), (C) BWO-0.1CN (red circles: Bi_2WO_6 ; yellow circles: $g\text{-C}_3\text{N}_4$), (D) HRTEM image and (E) EDS mapping of BWO-0.1CN.

3.2. Structure and Chemical Compositions of $\text{Bi}_2\text{WO}_6@g\text{-C}_3\text{N}_4$ Composites

The crystal structures of the Bi_2WO_6 , $g\text{-C}_3\text{N}_4$, BWO-0.05CN, BWO-0.1CN and BWO-0.15CN were evaluated using XRD analysis, respectively (Figure 3A). The main diffraction peaks of the Bi_2WO_6 nanoflower at 28.3° , 32.8° , 47.1° , 55.9° and 58.5° in the XRD pattern are indexed to the (131), (200), (202), (133) and (262) planes of the orthogonal Bi_2WO_6 phase

(JCPDS card No. 39-0256) [40]. The two peaks at 13.1° and 27.3° are the typical diffraction peaks of $g\text{-C}_3\text{N}_4$, which belong to the (100) and (002) planes of the C_3N_4 crystal [40]. However, there is no obvious peak of the $g\text{-C}_3\text{N}_4$ phase in a series of $\text{Bi}_2\text{WO}_6@g\text{-C}_3\text{N}_4$ heterostructure samples, which is probably due to the less content and low crystallinity of $g\text{-C}_3\text{N}_4$, and it overlaps with the strong peak of Bi_2WO_6 .

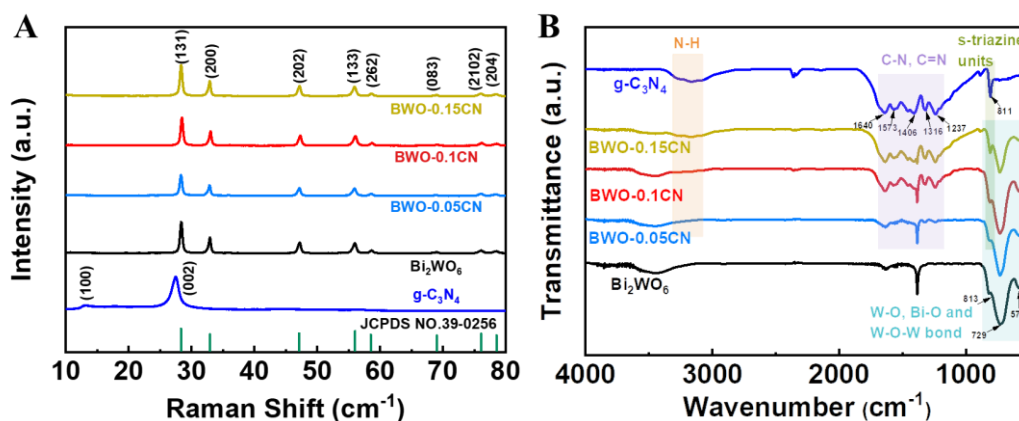


Figure 3. (A) XRD pattern and (B) FT-IR spectra of Bi_2WO_6 , $g\text{-C}_3\text{N}_4$, BWO-0.05CN, BWO-0.1CN, BWO-0.15CN (orange area: $3100\text{--}3300\text{ cm}^{-1}$; purple area: $1200\text{--}1650\text{ cm}^{-1}$; cyan area: $800\text{--}820\text{ cm}^{-1}$; mint tulip area: $500\text{--}820\text{ cm}^{-1}$).

Furthermore, the FT-IR spectra were carried out to investigate the chemical structure of the samples. As shown in Figure 3B, the broad peaks at $3100\text{--}3300\text{ cm}^{-1}$ (the orange area) are assigned to the N-H stretching vibration modes, which are mainly caused by the uncondensed amino groups in the $g\text{-C}_3\text{N}_4$. In addition, the absorption peaks at $1200\text{--}1650\text{ cm}^{-1}$ (the purple area) originate from the representative stretching modes of aromatic C-N and C=N heterocycles. And the featured typical peak located at 811 cm^{-1} is derived from the characteristic vibration mode of tri-s-triazine units [41]. Moreover, the vibration bands at 579 , 729 and 813 cm^{-1} in the Bi_2WO_6 sample could be attributed to the Bi-O, W-O and W-O-W bonds, respectively [42]. Obviously, it can be seen that the characteristic peaks of Bi_2WO_6 and $g\text{-C}_3\text{N}_4$ exist simultaneously in the series of $\text{Bi}_2\text{WO}_6@g\text{-C}_3\text{N}_4$ samples, demonstrating the successful construction of the $\text{Bi}_2\text{WO}_6@g\text{-C}_3\text{N}_4$ heterojunction.

The surface elemental compositions and valence states of the BWO-0.1CN sample were further confirmed through XPS measurements. As depicted in Figure 4A, the XPS survey spectrum of the BWO-0.1CN confirms the coexistence of Bi, W, O, C and N elements, in which the Bi, W and O elements come from the Bi_2WO_6 and the C and N elements due to the $g\text{-C}_3\text{N}_4$. Figure 4B–F show the high-resolution XPS spectra of Bi4f, W4f, O1s, C1s and N1s, respectively. The high-resolution of the Bi 4f spectra (Figure 4B) shows a pair of spin-orbit doublet peaks located at 164.67 and 159.38 eV , indicating that Bi exists in BWO-0.1CN in the form of Bi^{3+} [40]. As for the W4f core-level spectra (Figure 4C), two main peaks at binding energies of 37.76 and 35.63 eV were assigned to W $4f_{5/2}$ and W $4f_{7/2}$, respectively, suggesting that the W in BWO-0.1CN is in the valence state of W^{6+} [42]. In addition, the O 1s spectrum at 530.03 and 532.37 eV in Figure 4D is consistent with the different chemical environments of Bi-O and W-O for oxygen elements, and another peak at 530.57 eV corresponds to the OH^- group at the surface of Bi_2WO_6 . In Figure 4E, the C1s signal can be fitted into three peaks centered at 284.80 , 286.35 and 288.58 eV , which correspond to the graphitic carbon (C-C), sp^3 coordinated carbon (C-N₃) and sp^2 hybridized carbon (N-C=N), respectively [43]. Similarly, in the N1s spectrum (Figure 4F), the binding energies at 399.12 , 400.09 and 406.68 eV are attributed to the sp^2 hybridized nitrogen of C-N=C, the sp^3 bridged N atom of the N-C₃ group and the terminal amino groups of C-N-H, respectively [43]. Similarly, the different contents (5%, 15%) of $g\text{-C}_3\text{N}_4$ samples BWO-0.05CN and BWO-0.15CN show the adjacent parameters were used to deconvolute Bi4f, W4f, O1s, C1s and N1s core level as shown in Figures S1 and S2. Obviously, the

C-N₃ and N-C₃ groups in the C1s and N1s spectrum prove the existence of triple-s-triazine structure in g-C₃N₄, which also confirmed the coexistence of g-C₃N₄ and Bi₂WO₆ in the BWO-0.05CN, BWO-0.1CN and BWO-0.15CN heterojunction, and this is consistent with the results of the above measurements.

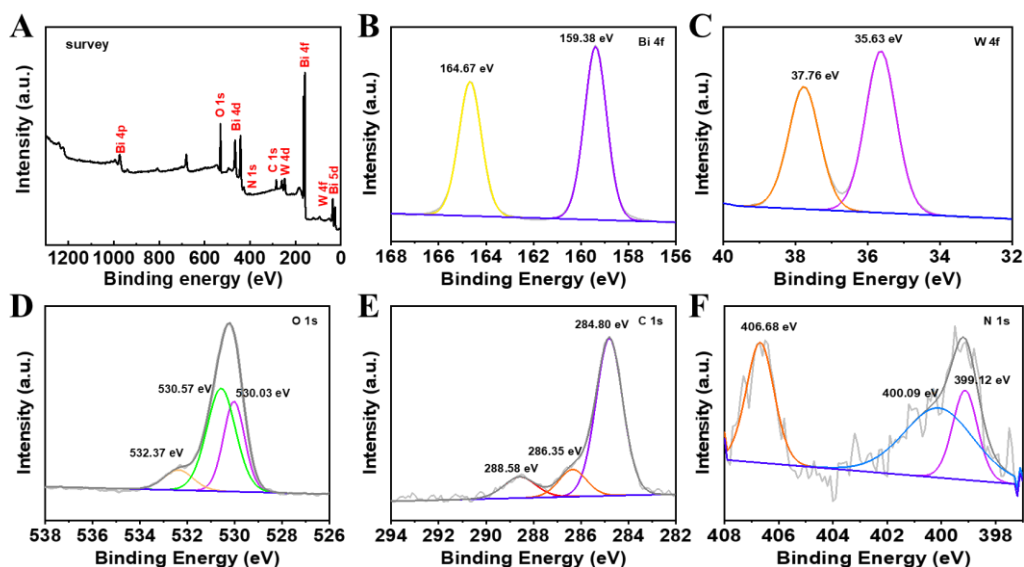


Figure 4. The XPS spectra of the BWO-0.1CN (A) Full scan, (B) Bi 4f, (C) W 4f, (D) O 1s, (E) C 1s, (F) N 1s.

3.3. Construction of the PEC Sensor

The transient photocurrent response of BWO/FTO and BWO-0.1CN/FTO in the presence and absence of DA under light irradiation was carried out in Figure 5A. Not surprisingly, the BWO/FTO shows a faint photocurrent intensity of about 32.5 nA in the absence of DA. Since g-C₃N₄ embedded in Bi₂WO₆ nanoflowers, the photocurrent value of BWO-0.1CN (78.7 nA) is stronger than BWO/FTO, and the absorption edge of BWO-0.1CN was between the pure Bi₂WO₆ and pure g-C₃N₄ (Figure S3A,B), indicating that the introduction of g-C₃N₄ nanosheets and the formation of Bi₂WO₆@g-C₃N₄ heterojunction are more susceptible to excitation. Likewise, in the presence of 50 μ M DA, the instantaneous photocurrent of BWO/FTO (250.9 nA) just accounted for 25.1% of BWO-0.1CN (999.3 nA). It should be pointed out that constructing a Bi₂WO₆@g-C₃N₄ heterostructure can more effectively hinder the recombination of carriers, thereby resulting in a remarkable photoelectric signal in return. EIS spectra of BWO/FTO and BWO-0.1CN/FTO are further authenticated by the viewpoint (Figure 5B), where BWO-0.1CN/FTO shows smaller semicircle radii with respect to BWO, indicating that BWO-0.1CN/FTO has a faster transfer rate of electrons.

To improve the fabricated sensor performance, the amounts of g-C₃N₄ nanosheets in Bi₂WO₆@g-C₃N₄ heterojunction were optimized, which are related to the transfer rate of carriers. Therefore, a series of composite materials BWO-0.05CN, BWO-0.1CN and BWO-0.15CN with different contents (5%, 10%, 15%) of g-C₃N₄ were synthesized. And the photocurrent response of these composites in the presence of 50 μ M DA was tested. From Figure S4A, it can be seen that as the doping ratio of g-C₃N₄ increases, the photocurrent response is gradually enhanced due to the more active sites that are beneficial for the capture of e⁻ or h⁺. Oppositely, the amount of g-C₃N₄ ratio exceeds 10%, and excessive g-C₃N₄ nanosheets cover the surface of the flower-like Bi₂WO₆, which limits the exposure of active sites, resulting in the photocurrent intensity presenting a downward trend. BWO-0.1CN exhibited the highest photocurrent response. Moreover, EIS spectra of BWO-0.05CN, BWO-0.1CN and BWO-0.15CN have further approved the impurity (Figure S4B), where BWO-0.1CN shows the smallest semicircle radii, indicating that BWO-0.1CN has the optimum conductivity. So we chose to construct the sensor with BWO-0.1CN as the photoelectrode

material. In addition, the parameter configuration is another factor that may trigger large differences in photocurrent response. Figure S4C depicts the influence of applied potential on the BWO-0.1CN-based sensor platform. The operation voltage of -0.2 V shows the strongest transient photoelectric current, but considering the ease of use in instrument integration, 0.0 V was chosen as the working voltage in the following experiment.

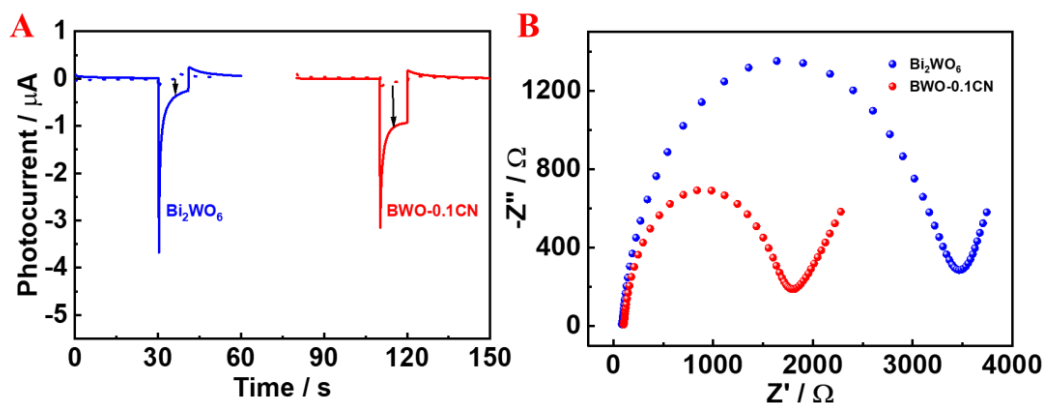


Figure 5. (A) Photocurrent response of BWO/FTO and BWO-0.1CN/FTO in the presence (solid line) and absence (dash line) of $50 \mu\text{M}$ DA at a bias potential of 0 V. (B) EIS spectra of BWO/FTO and BWO-0.1CN/FTO in 5 mM $[\text{Fe}(\text{CN})_6]^{3-/4-}$ containing 0.1 M KCl.

3.4. PEC Sensor for DA Detection

Relying on optimal experimental conditions, the PEC sensor fabricated based on BWO-0.1CN/FTO was used for the quantitative analysis of DA. As shown in Figure 6A, the photocurrent gradually increased with increasing the concentration of DA and eventually reached a plateau. As a matter of fact, there were two linear relationships between the concentration of DA and photocurrent intensity (Figure 6B). The linear ranges were $0.1\text{--}10 \mu\text{M}$ and $10\text{--}250 \mu\text{M}$, respectively. The linear equations were $y_1 = 44.47x_1 + 123.93$ ($R^2 = 0.9908$), $y_2 = 7.1188x_2 + 574.92$ ($R^2 = 0.9922$). It is worth noting that the slope was higher at a low concentration of DA because the electron transfer rate had greater change at a low concentration of DA compared to a high concentration [44,45]. And the detection limit was about 28 nM , which was comparable to the previously reported techniques (as shown in Table S1) [16,46–50]. Clearly, the established PEC sensor obtained excellent sensing performance for DA quantitative analysis.

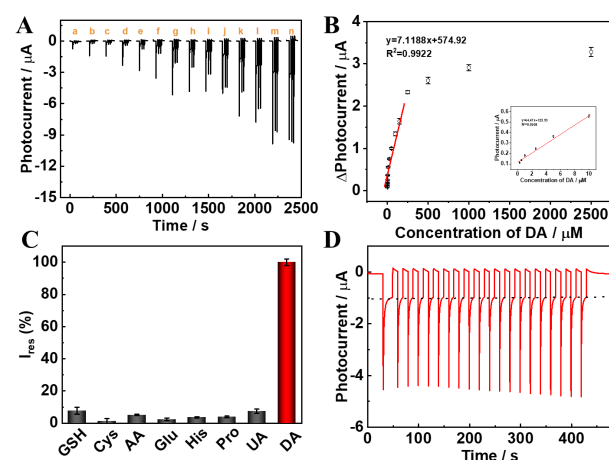


Figure 6. (A) PEC response of BWO-0.1CN/FTO in the presence of $0, 0.1, 0.5, 1.0, 2.5, 5.0, 10, 25, 50, 100, 150, 250, 500, 1000, 2500 \mu\text{M}$ DA (from curve a to curve n) in 0.1 M PBS ($\text{pH} = 7.40$) at a bias potential of 0 V. (B) Corresponding calibration curve for DA detection. (C) Selectivity of the proposed PEC sensor for DA. (D) Stability of BWO-0.1CN/FTO in the presence of $50 \mu\text{M}$ DA after scanning for 20 cycles.

3.5. Selectivity and Stability of the PEC Sensor

In fact, the actual test samples are more complex, and co-interferences may set obstacles to the detection process. In light of the actual requirement, the photocurrent responses of some possible commensal interferents (GSH, Cys, AA, Glu, His, Pro, UA) were compared with DA (Figure 6C), and it was observed that these interferents exhibited negligible PEC responses even at 10 times higher concentrations than DA. Furthermore, the interferer AA, which most readily interferes with DA detection, is only 7.4% of the DA photocurrent response at a tenfold concentration. The stability of the sensor constructed with BWO-0.1CN was verified with repeated irradiation on and off 20 times, with no significant photocurrent changes during the measurements, signifying acceptable stability (Figure 6D). These results indicated that the fabricated BWO-0.1CN-based sensor exhibited satisfactory selectivity and high photochemical stability.

3.6. Real Samples Analysis

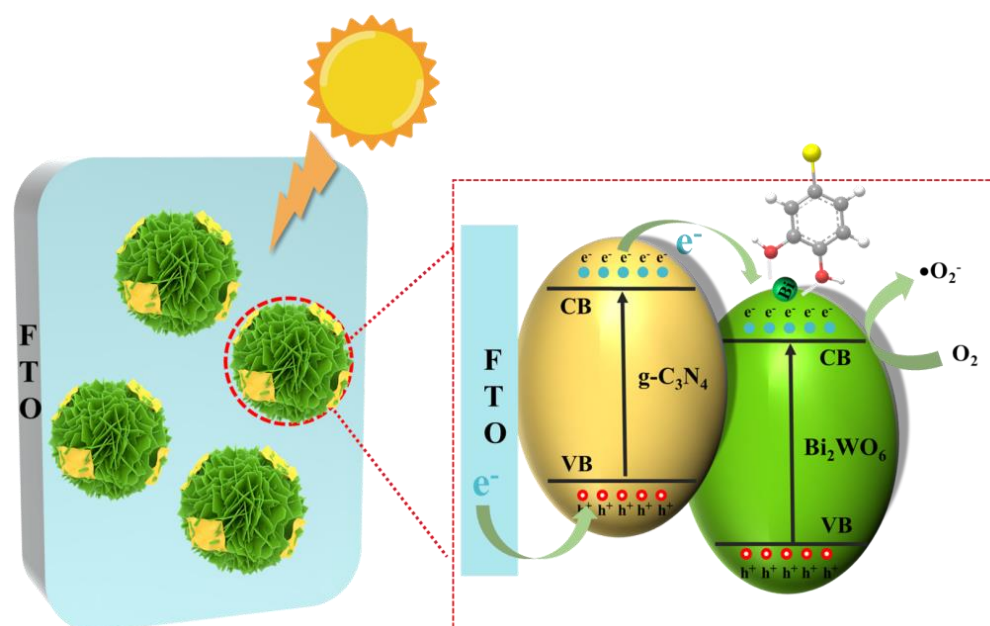
In order to investigate the practical application of the BWO-0.1CN-based PEC platform, the determination of DA in the human blood serum samples was carried out. The accuracy of the method was verified using the standard addition method, and DA standard solutions of 0.5 μM , 10 μM and 25 μM were adopted for the DA determination. The satisfactory recoveries (98.5–104%) and precision (RSD < 4%) were obtained from the assay results listed in Table 1, illustrating that the promising application of the BWO-0.1CN-based PEC sensor can be achieved for the detection of DA in real samples.

Table 1. PEC detection of DA in the human blood serum sample.

Analyte	Added (μM)	Found (μM)	Recovery (%)	RSD (%) (n = 3)
Human Blood serum	0.50	0.52	104.0	3.6
	10	10.14	101.4	1.4
	25	24.62	98.5	2.8

3.7. PEC Sensing Mechanism

Scheme 1 shows the possible mechanism for the selective detection of DA on the $\text{Bi}_2\text{WO}_6/\text{g-C}_3\text{N}_4/\text{FTO}$ electrode. When the BWO-0.1CN is irradiated with 420 nm light, electrons on the valence band (VB) of $\text{g-C}_3\text{N}_4$ can absorb photons and then transfer to the conduction band (CB) to generate e^- - h^+ pairs. Then, the photo-generated e^- is rapidly transferred to the CB of Bi_2WO_6 through the interface between $\text{g-C}_3\text{N}_4$ and Bi_2WO_6 . On the one hand, $\text{g-C}_3\text{N}_4$ nanosheets attached to 3D flower-like Bi_2WO_6 can not only reduce the diffusion pathway of photogenerated carriers participating in surface reactions but also facilitate the charge transfer in the heterojunction, resulting in enhanced photocurrent response. On the other hand, the abundant Bi^{3+} exposed on the Bi_2WO_6 surface may partially coordinate with water molecules due to the unstable bonding between Bi and O atoms [51]. More importantly, in the presence of DA, DA will replace water molecules and form the charge-transfer complex in concert with the exposed Bi^{3+} , leading to a change in the energy positions of the surface state [39]. Therefore, the free CB electrons react rapidly with the electron acceptor (dissolved O_2), which is a key factor for enhanced cathodic photocurrent. Thus, a PEC sensor for DA sensitive detection was developed based on the enhanced cathodic photocurrent strategy.



Scheme 1. Proposed PEC sensing mechanism for DA detection on the $\text{Bi}_2\text{WO}_6@\text{g-C}_3\text{N}_4/\text{FTO}$ photoelectrode.

4. Conclusions

In brief, a label-free cathodic PEC sensor employing BWO-0.1CN was simply established to achieve the sensitive and selective detection of DA. The introduction of $\text{g-C}_3\text{N}_4$ nanosheets and the formation of $\text{Bi}_2\text{WO}_6@\text{g-C}_3\text{N}_4$ heterojunctions are more susceptible to exciting and improving the transfer efficiency of photogenerated carriers. In addition, DA easily coordinates with exposed Bi^{3+} on the Bi_2WO_6 surface and forms the charge-transfer complex to further enhance the cathodic photocurrent. Benefitting from the $\text{Bi}_2\text{WO}_6@\text{g-C}_3\text{N}_4$ heterojunction interface, the proposed BWO-0.1CN-based analytical platform was successfully applied to the determination of DA with excellent interference resistance, high sensitivity, favorable reproducibility and good practicality. Such a simple and low-cost PEC platform holds great promise to apply for early DA-related disease diagnosis.

Supplementary Materials: The following supporting information can be downloaded at: <https://www.mdpi.com/article/10.3390/chemosensors11070404/s1>, Figure S1: The XPS spectra of the BWO-0.05CN (A) Full scan, (B) Bi 4f, (C) W 4f, (D) O 1s, (E) C 1s, (F) N 1s. Figure S2: The XPS spectra of the BWO-0.15CN (A) Full scan, (B) Bi 4f, (C) W 4f, (D) O 1s, (E) C 1s, (F) N 1s. Figure S3: (A) UV-vis diffuse reflectance absorption spectra, (B) the corresponding K-M plot of Bi_2WO_6 , $\text{g-C}_3\text{N}_4$, and BWO-0.1CN.; Figure S4: (A) Photocurrent response of BWO-0.05CN, BWO-0.1CN, and BWO-0.15CN in the presence of 50 μM DA. (B) Effects of the applied potential on photocurrent response of BWO-0.1CN/FTO electrode in 0.1 M PBS (pH = 7.4) containing 50 μM DA. Table S1: Comparison of previous and current DA detection methods. References [16,46–50] are cited in the Supplementary Materials.

Author Contributions: Conceptualization, Z.W.; methodology, Y.S. and F.H.; validation, Y.S. and F.H.; formal analysis, F.H. and D.Q.; investigation, Z.W. and Z.L.; data curation, Z.L.; writing—original draft preparation, D.H. and D.Q.; writing—review and editing, Z.W. and L.N.; supervision, L.N. All authors have read and agreed to the published version of the manuscript.

Funding: This research was funded by the National Key R&D Program of China (2022YFD2100304), National Natural Science Foundation of China (22172040, 21974031), University-Industry Collaborative Education Program of Ministry of Education of China (220605940231526), Guangdong Basic and Applied Basic Research Foundation (2023B1515040004), the Department of Science and Techniques of Guangdong Province (2021A1515010180, 2019B010933001), the Department of Guangdong Provincial Public Security (GZQC20-PZ11-FD084), Science and Technology Projects in Guangzhou (202201000002), Department of Science & Technology of Guangdong Province (ID:2022A156),

Guangzhou Municipal Science and Technology Bureau (202102010449) and Tertiary Education Scientific research project of Guangzhou Municipal Education Bureau (202235344), and we thank them for their financial support of this work.

Institutional Review Board Statement: Not applicable.

Informed Consent Statement: Not applicable.

Data Availability Statement: Not applicable.

Conflicts of Interest: The authors declare no conflict of interest.

References

1. Berke, J.D. What does dopamine mean? *Nat. Neurosci.* **2018**, *21*, 787–793. [[CrossRef](#)] [[PubMed](#)]
2. Zhang, Y.; Xu, M.; Gao, P.; Gao, W.; Bian, Z.; Jia, N. Photoelectrochemical sensing of dopamine using gold-TiO₂ nanocomposites and visible-light illumination. *Microchim. Acta* **2019**, *186*, 326. [[CrossRef](#)] [[PubMed](#)]
3. Liu, C.; Gomez, F.A.; Miao, Y.; Cui, P.; Lee, W. A colorimetric assay system for dopamine using microfluidic paper-based analytical devices. *Talanta* **2019**, *194*, 171–176. [[CrossRef](#)] [[PubMed](#)]
4. Segura-Aguilar, J.; Paris, I.; Munoz, P.; Ferrari, E.; Zecca, L.; Zucca, F.A. Protective and toxic roles of dopamine in Parkinson's disease. *J. Neurochem.* **2014**, *129*, 898–915. [[CrossRef](#)]
5. Faraone, S.V. The pharmacology of amphetamine and methylphenidate: Relevance to the neurobiology of attention-deficit/hyperactivity disorder and other psychiatric comorbidities. *Neurosci. Biobehav. Rev.* **2018**, *87*, 255–270. [[CrossRef](#)]
6. Guo, Z.; Seol, M.L.; Kim, M.S.; Ahn, J.H.; Choi, Y.K.; Liu, J.H.; Huang, X.J. Sensitive and selective electrochemical detection of dopamine using an electrode modified with carboxylated carbonaceous spheres. *Analyst* **2013**, *138*, 2683–2690. [[CrossRef](#)]
7. Zhuang, X.M.; Gao, X.Q.; Tian, C.Y.; Cui, D.L.; Luan, F.; Wang, Z.G.; Xiong, Y.; Chen, L.X. Synthesis of europium(iii)-doped copper nanoclusters for electrochemiluminescence bioanalysis. *Chem. Commun.* **2020**, *56*, 5755–5758. [[CrossRef](#)]
8. Peng, J.; Han, C.L.; Ling, J.; Liu, C.J.; Ding, Z.T.; Cao, Q.E. Selective fluorescence quenching of papain-Au nanoclusters by self-polymerization of dopamine. *Luminescence* **2018**, *33*, 168–173. [[CrossRef](#)] [[PubMed](#)]
9. Tsunoda, M.; Aoyama, C.; Nomura, H.; Toyoda, T.; Matsuki, N.; Funatsu, T. Simultaneous determination of dopamine and 3,4-dihydroxyphenylacetic acid in mouse striatum using mixed-mode reversed-phase and cation-exchange high-performance liquid chromatography. *J. Pharm. Biomed. Anal.* **2010**, *51*, 712–715. [[CrossRef](#)]
10. Shin, J.W.; Kim, K.J.; Yoon, J.; Jo, J.; El-Said, W.A.; Choi, J.W. Silver nanoparticle modified electrode covered by graphene oxide for the enhanced electrochemical detection of dopamine. *Sensors* **2017**, *17*, 2771. [[CrossRef](#)]
11. Zhou, J.; Huang, Y.; Chen, C.; Xiao, A.; Guo, T.; Guan, B.O. Improved detection sensitivity of gamma-aminobutyric acid based on graphene oxide interface on an optical microfiber. *Phys. Chem. Chem. Phys.* **2018**, *20*, 14117–14123. [[CrossRef](#)] [[PubMed](#)]
12. Kokulnathan, T.; Ahmed, F.; Chen, S.M.; Chen, T.W.; Hasan, P.M.Z.; Bilgrami, A.L.; Darwesh, R. Rational confinement of yttrium vanadate within three-dimensional graphene aerogel: Electrochemical analysis of monoamine neurotransmitter (dopamine). *ACS Appl. Mater. Interfaces* **2021**, *13*, 10987–10995. [[CrossRef](#)] [[PubMed](#)]
13. Yan, Y.; Liu, Q.; Du, X.; Qian, J.; Mao, H.; Wang, K. Visible light photoelectrochemical sensor for ultrasensitive determination of dopamine based on synergistic effect of graphene quantum dots and TiO₂ nanoparticles. *Anal. Chim. Acta* **2015**, *853*, 258–264. [[CrossRef](#)] [[PubMed](#)]
14. Hun, X.; Wang, S.; Wang, S.; Zhao, J.; Luo, X. A photoelectrochemical sensor for ultrasensitive dopamine detection based on single-layer NanoMoS₂ modified gold electrode. *Sens. Actuators B Chem.* **2017**, *249*, 83–89. [[CrossRef](#)]
15. Ma, W.; Wang, L.; Zhang, N.; Han, D.; Dong, X.; Niu, L. Biomolecule-free, selective detection of o-diphenol and its derivatives with WS₂/TiO₂-based photoelectrochemical platform. *Anal. Chem.* **2015**, *87*, 4844–4850. [[CrossRef](#)]
16. Wu, Z.; Han, F.; Wang, T.; Guan, L.; Liang, Z.; Han, D.; Niu, L. A recognition-molecule-free photoelectrochemical sensor based on Ti₃C₂/TiO₂ heterostructure for monitoring of dopamine. *Biosensors* **2023**, *13*, 526. [[CrossRef](#)]
17. Han, F.J.; Song, Z.Q.; Xu, J.N.; Dai, M.J.; Luo, S.L.; Han, D.X.; Niu, L.; Wang, Z.X. Oxidized titanium carbide MXene-enabled photoelectrochemical sensor for quantifying synergistic interaction of ascorbic acid based antioxidants system. *Biosens. Bioelectron.* **2021**, *177*, 112978. [[CrossRef](#)]
18. Zhang, J.; Huang, L.; Jin, H.; Sun, Y.; Ma, X.; Zhang, E.; Wang, H.; Kong, Z.; Xi, J.; Ji, Z. Constructing two-dimension MoS₂/Bi₂WO₆ core-shell heterostructure as carriers transfer channel for enhancing photocatalytic activity. *Mater. Res. Bull.* **2017**, *85*, 140–146. [[CrossRef](#)]
19. Li, C.; Chen, G.; Sun, J.; Feng, Y.; Liu, J.; Dong, H. Ultrathin nanoflakes constructed erythrocyte-like Bi₂WO₆ hierarchical architecture via anionic self-regulation strategy for improving photocatalytic activity and gas-sensing property. *Appl. Catal. B* **2015**, *163*, 415–423. [[CrossRef](#)]
20. Zhang, Z.J.; Wang, W.Z.; Wang, L.; Sun, S.M. Enhancement of visible-light photocatalysis by coupling with narrow-band-gap semiconductor: A case study on Bi₂S₃/Bi₂WO₆. *ACS Appl. Mater. Interfaces* **2012**, *4*, 593–597. [[CrossRef](#)]
21. Li, C.; Chen, G.; Sun, J.; Rao, J.; Han, Z.; Hu, Y.; Zhou, Y. A novel mesoporous single-crystal-like Bi₂WO₆ with enhanced photocatalytic activity for pollutants degradation and oxygen production. *ACS Appl. Mater. Interfaces* **2015**, *7*, 25716–25724. [[CrossRef](#)] [[PubMed](#)]

22. Zhang, L.; Wang, W.; Zhou, L.; Xu, H. Bi₂WO₆ nano and microstructures: Shape control and associated visible-light-driven photocatalytic activities. *Small* **2007**, *3*, 1618–1625. [[CrossRef](#)] [[PubMed](#)]
23. Zhang, L.; Wang, W.; Chen, Z.; Zhou, L.; Xu, H.; Zhu, W. Fabrication of flower-like Bi₂WO₆ superstructures as high performance visible-light driven photocatalysts. *J. Mater. Chem.* **2007**, *17*, 2526–2532. [[CrossRef](#)]
24. Qi, S.; Zhang, R.; Zhang, Y.; Liu, X.; Xu, H. Preparation and photocatalytic properties of Bi₂WO₆/g-C₃N₄. *Inorg. Chem. Commun.* **2021**, *132*, 108761. [[CrossRef](#)]
25. Liu, J.; Wang, T.; Nie, Q.; Hu, L.; Cui, Y.; Tan, Z.; Yu, H. One-step synthesis of metallic Bi deposited Bi₂WO₆ nanoclusters for enhanced photocatalytic performance: An experimental and DFT study. *Appl. Surf. Sci.* **2021**, *559*, 149970. [[CrossRef](#)]
26. Liu, L.; Liu, J.; Sun, K.; Wan, J.; Fu, F.; Fan, J. Novel phosphorus-doped Bi₂WO₆ monolayer with oxygen vacancies for superior photocatalytic water detoxication and nitrogen fixation performance. *Chem. Eng. J.* **2021**, *411*, 128629. [[CrossRef](#)]
27. Peng, J.; Zhuge, W.; Liu, Y.; Zhang, C.; Yang, W.; Huang, Y. Photoelectrochemical dopamine sensor Based on Cu-Doped Bi₂WO₆ micro-Flowers sensitized cobalt tetraaminophthalocyanine functionalized graphene oxide. *J. Electrochem. Soc.* **2019**, *166*, B1612–B1619. [[CrossRef](#)]
28. Wang, X.; Rong, X.; Zhang, Y.; Luo, F.; Qiu, B.; Wang, J.; Lin, Z. Homogeneous photoelectrochemical aptasensors for tetracycline based on sulfur-doped g-C₃N₄/n-GaN heterostructures formed through self-assembly. *Anal. Chem.* **2022**, *94*, 3735–3742. [[CrossRef](#)]
29. Liu, Z.; Zhou, Y.; Yang, L.; Yang, R. Green preparation of in-situ oxidized TiO₂/Ti₃C₂ heterostructure for photocatalytic hydrogen production. *Adv. Powder Technol.* **2021**, *32*, 4857–4861. [[CrossRef](#)]
30. Zhang, J.; Shang, M.; Gao, Y.; Yan, J.; Song, W. High-performance VS₂ QDs-based type II heterostructured photoanode for ultrasensitive aptasensing of lysozyme. *Sens. Actuators B Chem.* **2020**, *304*, 127411. [[CrossRef](#)]
31. Adhikari, S.; Kim, D.-H. Synthesis of Bi₂S₃/Bi₂WO₆ hierarchical microstructures for enhanced visible light driven photocatalytic degradation and photoelectrochemical sensing of ofloxacin. *Chem. Eng. J.* **2018**, *354*, 692–705. [[CrossRef](#)]
32. Zhang, M. Synthesis of Bi₂WO₆/TiO₂ flake nano-heterostructure photocatalyst and its photocatalytic performance under visible light irradiation. *J. Mater. Sci. Mater. Electron.* **2020**, *31*, 20129–20138. [[CrossRef](#)]
33. Zhao, B.; Luo, Y.; Qu, X.; Hu, Q.; Zou, J.; He, Y.; Liu, Z.; Zhang, Y.; Bao, Y.; Wang, W.; et al. Graphite-like carbon nitride nanotube for electrochemiluminescence featuring high efficiency, high stability, and ultrasensitive ion detection capability. *J. Phys. Chem. Lett.* **2021**, *12*, 11191–11198. [[CrossRef](#)]
34. Yang, H.; Zhou, Q.; Fang, Z.; Li, W.; Zheng, Y.; Ma, J.; Wang, Z.; Zhao, L.; Liu, S.; Shen, Y.; et al. Carbon nitride of five-membered rings with low optical bandgap for photoelectrochemical biosensing. *Chem* **2021**, *7*, 2708–2721. [[CrossRef](#)]
35. Wang, D.; Li, J.; Xu, Z.; Zhu, Y.; Chen, G.; Cui, Z. Synthesis of g-C₃N₄/NiO p–n heterojunction materials with ball-flower morphology and enhanced photocatalytic performance for the removal of tetracycline and Cr⁶⁺. *J. Mater. Sci.* **2019**, *54*, 11417–11434. [[CrossRef](#)]
36. Zhao, Z.; Wu, Z.; Lin, X.; Han, F.; Liang, Z.; Huang, L.; Dai, M.; Han, D.; Han, L.; Niu, L. A label-free PEC aptasensor platform based on g-C₃N₄/BiVO₄ heterojunction for tetracycline detection in food analysis. *Food Chem.* **2023**, *402*, 134258. [[CrossRef](#)]
37. Cao, Y.; Wang, L.; Wang, C.; Hu, X.; Liu, Y.; Wang, G. Sensitive detection of glyphosate based on a Cu-BTC MOF/g-C₃N₄ nanosheet photoelectrochemical sensor. *Electrochim. Acta* **2019**, *317*, 341–347. [[CrossRef](#)]
38. Xu, Y.; Yu, S.; Zhu, Y.; Fan, G.; Han, D.; Qu, P.; Zhao, W. Cathodic photoelectrochemical bioanalysis. *TrAC Trend. Anal. Chem.* **2019**, *114*, 81–88. [[CrossRef](#)]
39. Weng, S.; Hu, J.; Lu, M.; Ye, X.; Pei, Z.; Huang, M.; Xie, L.; Lin, S.; Liu, P. In situ photogenerated defects on surface-complex BiOCl (0 1 0) with high visible-light photocatalytic activity: A probe to disclose the charge transfer in BiOCl (0 1 0)/surface-complex system. *Appl. Catal. B* **2015**, *163*, 205–213. [[CrossRef](#)]
40. Yang, C.; Chai, H.; Xu, P.; Wang, P.; Wang, X.; Shen, T.; Zheng, Q.; Zhang, G. One-step synthesis of a 3D/2D Bi₂WO₆/g-C₃N₄ heterojunction for effective photocatalytic degradation of atrazine: Kinetics, degradation mechanisms and ecotoxicity. *Sep. Purif. Technol.* **2022**, *288*, 120609. [[CrossRef](#)]
41. Wang, Q.; Wang, W.; Zhong, L.; Liu, D.; Cao, X.; Cui, F. Oxygen vacancy-rich 2D/2D BiOCl-g-C₃N₄ ultrathin heterostructure nanosheets for enhanced visible-light-driven photocatalytic activity in environmental remediation. *Appl. Catal. B* **2018**, *220*, 290–302. [[CrossRef](#)]
42. Zhu, D.; Zhou, Q. Novel Bi₂WO₆ modified by N-doped graphitic carbon nitride photocatalyst for efficient photocatalytic degradation of phenol under visible light. *Appl. Catal. B* **2020**, *268*, 118426. [[CrossRef](#)]
43. Duan, Y.; Li, X.; Lv, K.; Zhao, L.; Liu, Y. Flower-like g-C₃N₄ assembly from holy nanosheets with nitrogen vacancies for efficient NO abatement. *Appl. Surf. Sci.* **2019**, *492*, 166–176. [[CrossRef](#)]
44. Zheng, L.; Zhang, H.; Won, M.; Kim, E.; Li, M.; Kim, J.S. Codoping g-C₃N₄ with boron and graphene quantum dots: Enhancement of charge transfer for ultrasensitive and selective photoelectrochemical detection of dopamine. *Biosens. Bioelectron.* **2023**, *224*, 115050. [[CrossRef](#)]
45. Kong, W.; Zhu, D.; Luo, R.; Yu, S.; Ju, H. Framework-promoted charge transfer for highly selective photoelectrochemical biosensing of dopamine. *Biosens. Bioelectron.* **2022**, *211*, 114369. [[CrossRef](#)]
46. Peng, J.; Li, X.; Liu, Y.; Zhuge, W.; Zhang, C.; Huang, Y. Photoelectrochemical sensor based on zinc phthalocyanine semiconducting polymer dots for ultrasensitive detection of dopamine. *Sens. Actuators B Chem.* **2022**, *360*, 131619. [[CrossRef](#)]

47. Chen, Y.; Li, X.; Cai, G.; Li, M.; Tang, D. In situ formation of (001)TiO₂/Ti₃C₂ heterojunctions for enhanced photoelectrochemical detection of dopamine. *Electrochem. Commun.* **2021**, *125*, 106987. [[CrossRef](#)]
48. Yao, W.; Guo, H.; Liu, H.; Li, Q.; Xue, R.; Wu, N.; Li, L.; Wang, M.; Yang, W. Simultaneous electrochemical determination of acetaminophen and dopamine based on metal-organic framework/multiwalled carbon nanotubes-Au@Ag nanocomposites. *J. Electrochem. Soc.* **2019**, *166*, B1258–B1267. [[CrossRef](#)]
49. Liu, S.; Shi, F.; Zhao, X.; Chen, L.; Su, X. 3-Aminophenyl boronic acid-functionalized CuInS₂ quantum dots as a near-infrared fluorescence probe for the determination of dopamine. *Biosens. Bioelectron.* **2013**, *47*, 379–384. [[CrossRef](#)]
50. Hao, Q.; Wang, P.; Ma, X.; Su, M.; Lei, J.; Ju, H. Charge recombination suppression-based photoelectrochemical strategy for detection of dopamine. *Electrochem. Commun.* **2012**, *21*, 39–41. [[CrossRef](#)]
51. Moser, J.; Punchedewa, S.; Infelta, P.P.; Graetzel, M. Surface complexation of colloidal semiconductors strongly enhances interfacial electron-transfer rates. *Langmuir* **1991**, *7*, 3012–3018. [[CrossRef](#)]

Disclaimer/Publisher's Note: The statements, opinions and data contained in all publications are solely those of the individual author(s) and contributor(s) and not of MDPI and/or the editor(s). MDPI and/or the editor(s) disclaim responsibility for any injury to people or property resulting from any ideas, methods, instructions or products referred to in the content.